ChemPhysChem

Research Article
doi.org/10.1002/cphc.202300197

Chemistry Europe
European Chemical
Societies Publishing

www.chemphyschem.org

Tailored Porous Transport Layers for Optimal Oxygen Transport in Water Electrolyzers: Combined Stochastic Reconstruction and Lattice Boltzmann Method

Jiang Liu,[a] Min Li,[b, c] Yingying Yang,[a] Nicolas Schlüter,[a] Dajan Mimic,[b, c] and Daniel Schröder*[a, d]

The porous transport layer (PTL) plays an integral role for the mass transport in polymer electrolyte membrane (PEM) electrolyzers. In this work, a stochastic reconstruction method of titanium felt-based PTLs is applied and combined with the Lattice Boltzmann method (LBM). The aim is to parametrically investigate the impact of different PTL structures on the transport of oxygen. The structural characteristics of a reconstructed PTL agree well with experimental investigations. Moreover, the impact of PTL porosity, fiber radius, and anisotropy parameter on the structural characteristics of PTLs are analyzed, and their impact on oxygen transport are elucidated by LBM. Eventually, a customized graded PTL is reconstructed, exhibiting almost optimal mass transport performance for the removal of oxygen. The results show that a higher porosity, larger fiber radius, and smaller anisotropy parameter facilitate the formation of oxygen propagation pathways. By tailoring the fiber characteristics and thus optimizing the PTLs, guidelines for the optimal design and manufacturing can be obtained for large-scale PTLs for electrolyzers.

Introduction

Anthropogenic climate change is driving a growing number of countries and corporations to commit to net zero carbon emissions by 2050.[1] In the decarbonization process, green hydrogen produced by water electrolysis will play an essential role.[2] Among various water electrolysis technologies, polymer electrolyte membrane electrolysis (PEMEC) has attracted considerable attention due to its high current density, rapid response time during start/shutdown, compact design, and high efficiency.[3,4]

The PEM electrolyzer splits water into oxygen and hydrogen under an external electrical power, acting as an electrochemical energy conversion device. Figure 1a shows the schematic of a PEM electrolysis cell, and (b) shows the simplified triple-phases in a cell. Typically, a PEM electrolysis cell consists of a polymer
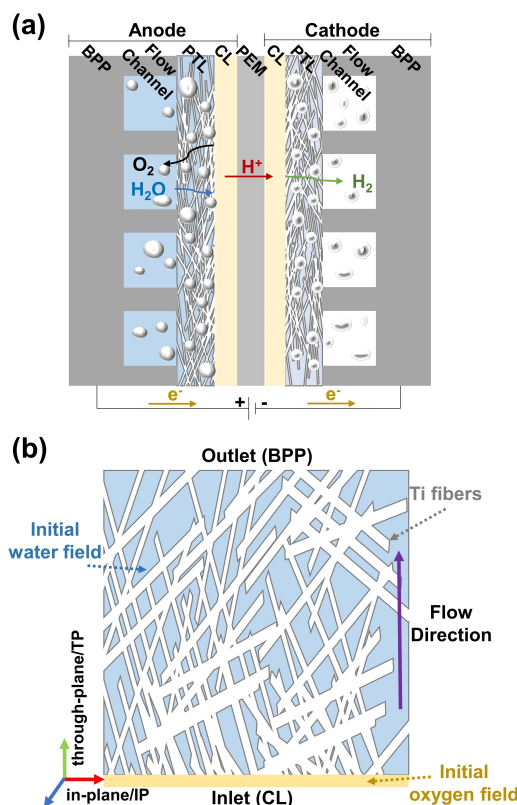
[a] J. Liu, Y. Yang, Dr. N. Schlüter, Prof. D. Schröder
     Institute of Energy and Process Systems Engineering,
     Technische Universität Braunschweig,
     Langer Kamp 19B, 38106 Braunschweig, Germany
     E-mail: d.schroeder@tu-braunschweig.de
[b] M. Li, Dr. D. Mimic
     Cluster of Excellence SE²A – Sustainable and Energy-Efficient Aviation,
     Technische Universität Braunschweig,
     38108 Braunschweig, Germany
[c] M. Li, Dr. D. Mimic
     Institute of Turbomachinery and Fluid Dynamics,
     Leibniz Universität Hannover,
     An der Universität 1, 30823 Garbsen, Germany
[d] Prof. D. Schröder
     Battery LabFactory Braunschweig (BLB),
     Technische Universität Braunschweig,
     Langer Kamp 19, 38106 Braunschweig, Germany

Figure 1. Schematic of a) a PEM electrolysis cell and b) the boundary conditions implemented in simulations.

ChemPhysChem

Research Article
doi.org/10.1002/cphc.202300197

Chemistry Europe
European Chemical
Societies Publishing

electrolyte membrane (PEM), catalyst layers (CLs), porous transport layers (PTLs), flow channels, and bipolar plates (BPPs). The PEM and CLs together make up the catalyst-coated membrane (CCM). On the anode side, liquid water is supplied to the flow channels of the bipolar plates and then travels through the PTL to the catalyst layer, where the water is split to generate oxygen and protons. The product oxygen, generated at the anode, needs to be dissipated through the PTL and removed from the flow channel. The protons pass through the membrane to the cathode where they are reduced to hydrogen. The reactions occurring at the anode and the cathode are as follows [Eq. (1) and (2)]:

$$H_2O \rightarrow 2H^+ + \frac{1}{2}O_2 + 2e^- \ (\text{Anode}) \quad (1)$$

$$2H^+ + 2e^- \rightarrow H_2 \ (\text{Cathode}) \quad (2)$$

The anodic PTL plays a crucial role in PEM electrolyzers. It provides pathways for the transport of the reactant water and the product oxygen, maintains proper electrical and thermal conductivity, and also provides mechanical support.[5] The structure of the PTLs affects the mass transport losses and ohmic losses of electrolyzers. An unreasonable design will cause flow obstructions of the reactant and product, and a reduction in available electrochemically active sites,[6–8] especially when PEM electrolyzers are operated at high current densities.

The high potential and corrosive environment resulting from the electrochemical reaction at the anode make the use of materials like Titanium obligatory for the anodic PTL.[6] Among several types of titanium-based PTLs, such as the Ti felt,[9–11] sintered Ti powder,[12,13] and Ti mesh,[14,15] the felt-based PTL attracted significant attentions due to its flexible porosity, fiber size, and thickness.[16]

In order to understand the impact of the PTL structure on the mass transport and efficiency of PEM electrolyzers, numerous research methods have emerged in recent years, including electrochemical experiments,[17–21] visualization experiments,[22–25] macroscale modeling,[26–29] and mesoscopic scale simulations.[30–32]

Suermann et al.[12] studied the effect of current density, operating pressure, and temperature on mass transport overpotential. They correlated the results with PTL structural features characterized by X-ray Tomographic Microscopy (XTM) such as porosity, pore and solid size distribution (PSD and SSD), and effective transport properties. Their results show that the transport losses decrease with increasing operating pressure and temperature, and show a strong correlation with PTL structural properties. Kim et al.[33] investigated the mass transport in PTLs with straight pores in the through-plane direction via X-ray radiography and electrochemical analysis, finding that water cannot access the pores under the ribs and that limited in-plane mass transport can lead to dehydration of the CL. To reduce the activation overpotential, Wang et al.[34] applied a new method to remove oxygen bubbles from the reaction sites on the catalyst layers by using a magnet. By controlling the magnetic field, it is possible to realize the directional migration of oxygen bubbles. The bubble shedding can be accelerated by

increasing the magnetic strength. Schuler et al.[10,21] characterized the morphology and topology representing the bulk properties of different PTLs by XTM, calculated transport parameters, and performed electrochemical analysis, which revealed the correlation between PTL structural properties and the performance of PEM electrolyzers through a detailed electrochemical loss breakdown.

Ito et al.[35] conducted an experimental study regarding the impact of structural properties such as porosity and pore size of PTLs on the performance of PEM electrolyzers. They concluded that a smaller mean pore size is beneficial to improve the performance when the mean pore size of the PTLs is larger than 10 μm. Once the porosity exceeds 0.50, there is no significant impact of the pore size on the performance anymore. A novel PTL produced by vacuum plasma spraying (VPS) was presented in the study by Lettenmeier et al.[20] This PTL has a gradient distribution of porosity along the through-plane direction, with a pore radius of 10 μm near the bipolar plate and 5 μm at the interface with the catalyst layer, which can achieve the performance comparable to state-of-the-art sintered plates. The work by Grigoriev et al.[27] focused on optimizing the PTL microstructure to have efficient electric contact and gas/water transport. Zielke et al.[9] reconstructed eight different PTLs via X-ray tomography, and exponential relations between through-plane thermal conductivity and porosity, as well as between through-plane electrical conductivity and water permeability were determined. In the work of Hwang et al.,[18] the PSD of a PTL was changed by loading titanium powder into the PTL to evaluate water management. All of the aforementioned works targeted the trade-off between the optimal PTL structure for mass transport and minimal electrochemical losses for the ongoing reactions.

Simulation methods make it possible to obtain spatiotemporal information about the two-phase distribution within the PTLs. Lee et al. proposed a stochastic modeling method to reconstruct sintered powder-based PTLs by using geometrical data from XTM. They compared the surface morphology and structural properties of the reconstructed PTL with the experimental PTL[36] and investigated the effect of powder diameter and porosity on mass transport[37] as well as the PEMEC performance under special conditions.[19] Jung et al.[13] used XTM and mercury intrusion porosimetry (MIP) to characterize the microstructure of different PTL materials, and compared the transport properties with those obtained by direct numerical simulation (DNS) and pore network modeling (PNM) methods. In addition, the Lattice Boltzmann method (LBM) and some other methods (such as the Finite Element Method and Finite Volume Method) as well as comparative studies between those methods have also been applied in some works to numerically study oxygen bubble dynamics in PTLs and other porous structures.[30,31,38–42]

The application of neutron-based imaging provides the possibility to visualize the mass transport process in PTLs. Neutron radiography and optical imaging technology were applied to obtain the distribution and film thickness of water in the PTL, exploring the effects of current density, water supply (i.e., the flow rate of water), and temperature.[24,43] Lee et al.[44]

ChemPhysChem

Research Article
doi.org/10.1002/cphc.202300197

**Chemistry
Europe**
European Chemical
Societies Publishing

examined spatially graded PTLs and revealed a great perform-ance improvement of PEM electrolyzers brought by the high to low porosity distribution of PTLs along the flow channels to catalyst layers direction. The approach leads to a 38% reduction in mass transport overpotential at a current density of 4.5 A/cm^2, indicating the great potential for custom-graded PTLs to enhance the electrolyzer performance. Li et al.[45] experimentally investigated the oxygen bubble dynamics and two-phase flow in PTLs with straight-through pores by using a specifically designed transparent PEMEC and evaluated the effect of operating conditions on the oxygen bubble dynamics in the channels and pores, as well as the flow regime transformation. As the temperature and/or current density increases, the nucleation site, growth rate, and number of oxygen bubbles increase as well. The microfluidic platform is a 2-D representa-tion of porous structures used to visualize the multiphase flow behavior within the porous media. In the work of Arbabi[23] and Lee[46] et al., this platform was used for the visualization of bubble transport in 2-D PTLs to understand the relationship between the structural properties of PTLs and the two-phase distribution. The work of Swiegers et al. reviewed innovative strategies for eliminating or mitigating bubble effects to improve the efficiency and cost of water electrolyzers.[47]

Although a large variety of studies has been conducted so far, many of them were limited to costly and time-consuming experimental and 2-D numerical studies. The much more complex 3-D temporal and spatial two-phase distributions inside PTLs cannot be obtained with the latter. Most of the current work considered the direct relationship between PTL structural properties and PEMEC performance,[12,29,48–50] but the necessary and important correlations between the pore-scale structure and mass transport are still missing, as concluded in the latest work of Bhaskaran et al.[51] In their work, they numerically investigated the oxygen propagation inside graded PTLs in relation to the structural properties, indicating a strong dependence of the two-phase flow behaviors on the graded structure. The porosity and pore structural properties of PTLs are critical to the mass transport losses and ohmic losses of PEMECs. A higher porosity is beneficial for a fast transport of oxygen produced by the oxygen evolution reaction (OER) at the catalyst layer through the PTL. At the same time, a higher porosity will increase the ohmic losses.[16,21] Therefore, the selection of PTL structures is a very contradictory and intract-able problem, and this work will focus on the impact of PTL structural properties on the distribution of gas/water within this layer, aiming to provide more perspectives for the design and application of PTLs. Inspired by the work of Bhaskaran et al.,[51] an optimal graded PTL structure is targeted in our work while other structural details of the PTL, such as the porosity, fiber radius, and fiber orientation are fully considered.

We herein present both a stochastically numerical recon-struction method and the LBM. The aim is to obtain the oxygen propagation inside the PTLs with varied structural properties. Firstly, the experimental PTL structure from the literature[10] is reconstructed, and the key structural parameters and the PSD of the reconstructed and experimental PTLs are compared to determine the validity of the method. Subsequently, a series of

PTLs with different porosity, fiber radii, and anisotropy parame-ters are reconstructed, and the impact of different structural properties on the internal structure of PTLs is analyzed in detail. Then, the two-phase distributions are obtained through LBM simulations to correlate the PTL structure and the transport of oxygen. Finally, a customized graded PTL structure is recon-structed based on the results to obtain the optimal ability to remove oxygen. The presented results not only help understand the essential relationship between the PTL structure and the transport of oxygen, but also provide access to guidelines for the design and application of PTLs in the future.

Methodology

Stochastically Numerical 3-D Structure Reconstruction

The felt-based PTLs considered herein usually consist of Ti fibers, as shown in Figure 2a.[52] Based on available data in the literature and online by the manufacturer (Bekaert), the typical porosity of Ti felt PTLs is in the range of 0.40–0.90, the fiber diameter 10 μm–50 μm, and the thickness 100 μm–2 mm.[9,10] To generate the virtual PTLs with customized structures, a stochastic reconstruction algorithm implemented in MATLAB R2021b was applied, based on well-described methods from literature.[53–55] Figure 2b shows the flow chart of the generation of a titanium felt-based PTL within this work. In order to customize the structural characteristics of stochastically gener-ated PTLs, the PTL structural parameters need to be input in the code, including matrix domain size, porosity, fiber radius, fiber length, and anisotropy parameter. Fibers with a given radius are then generated within the domain until the target porosity is satisfied.

To simplify the reconstruction process, the following assumptions are made: a) The fibers are long-straight cylindrical; b) All fibers share the same, fixed radius; c) During the generation process, the fibers are allowed to cross and overlap with each other; d) Only fibers and pores are present within the PTL.

In this work, various PTLs with different structural parame-ters were reconstructed by using the aforementioned stochastic reconstruction method. In order to achieve control of only a single variable, all other structural parameters were kept constant when reconstructing the PTLs with different porosity ε/fiber radii r_{fiber}/anisotropy parameters β. As shown in Fig-ure 2c,d, PTLs with different porosity comprise the same fiber radius of 5.0 μm, which is close to the experimental value of 5.5 μm,[10] and PTLs with different fiber radii comprise the same porosity of 0.74 for the purpose of observing the two-phase behavior within the high-porosity PTL and reducing the computational cost. The application of thin PTL requires the use of small size fibers to avoid concerns such as inadequate interfacial contact.[10] For the PTLs with different porosity and fiber radii, the fibers are all stacked in the $x - z$ (in-plane) coordinate system. Thus, the reconstructed PTL structures possess a strong anisotropy in the x, z, and y directions. In the stochastic reconstruction algorithm, fibers can also be arranged

ChemPhysChem

Research Article
doi.org/10.1002/cphc.202300197

Chemistry Europe
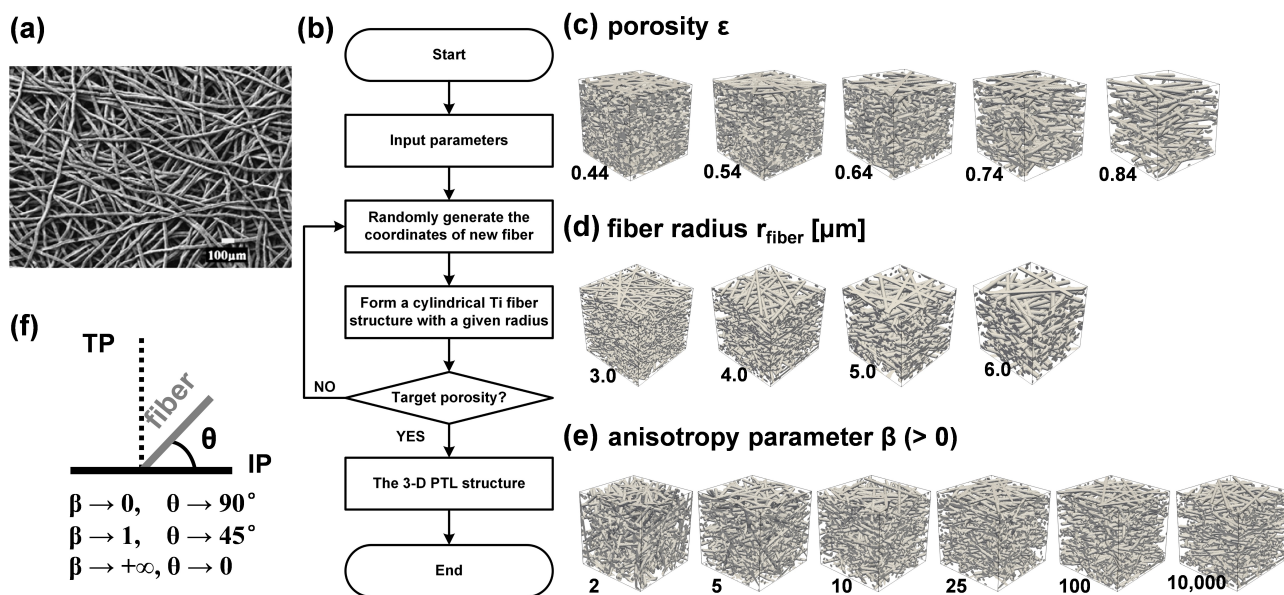European Chemical
Societies Publishing

Figure 2. a) SEM image of Ti felt PTL (Bekinit) (this figure has been reproduced from Ref. [52] with permission from Elsevier, copyright 2011). b) The steps for a 3-D PTL reconstruction, c)-e) 3-D renderings of the reconstructed PTLs ($200 \times 200 \times 200$ μm^3) with different porosity (ε), fiber radii (r_{fiber}), and anisotropy parameters (β), f) the functional description of anisotropy parameter β.

in the through-plane (y) direction following the probability density function [Eq. (3)]:[56]

$$p_y(\theta) = \frac{1}{4\pi} \frac{\beta \sin\theta}{(1+(\beta^2-1)\cos^2\theta)^{3/2}} \tag{3}$$

where β is called the anisotropy parameter, which controls the orientation of the fibers, and θ is the polar angle of the Ti fiber. As shown in Figure 2f, the anisotropy parameter governs the preferential orientation of the fibers according to equation (3). When β approaches the value of unity, the fibers' orientation will be uniformly distributed in the $x-y-z$ direction. As β approaches zero, more fibers will be parallel to the through-plane direction and as β increases, more fibers will orient in the in-plane direction. Figure 2e shows the reconstructed PTLs comprising different anisotropy parameters, with a porosity of 0.74 and a fiber radius of 4.0 μm.

Lattice Boltzmann Method

The traditional Computational Fluid Dynamics (CFD) method is based on the continuum assumption and uses numerical analysis techniques to solve the Navier-Stokes equation; while the LBM simulates the fluid through the discrete Boltzmann equations at a more fundamental dynamic level.[57] The multiple relaxation time (MRT) LBM is implemented in this study to solve for the transport of oxygen in the PTL.[58,59] Within the PTL, oxygen, water, and solid fibers form a three-phase system, which is governed by the Navier-Stokes equations and the Cahn-Hilliard equation [Eq. (4) and (5)]:

$$\frac{\partial \rho u}{\partial t} + \nabla \cdot \rho uu = -\nabla \cdot p + \eta \nabla^2 u + F \tag{4}$$

$$\frac{\partial \varphi}{\partial t} + \nabla \cdot \varphi u = M \nabla^2 \mu \tag{5}$$

In the equations, ρ, u, t represent the density, velocity, and time respectively, p, η, F represent the pressure tensor, viscosity, and the body force, and φ, M, μ represent the order parameter, mobility, and the chemical potential. The two equations above can also be solved by the following Equations (6) and (7):

$$f_i(r+e_i\delta t, t+\delta t) = f_i(r,t) - \mathcal{Q}^{-1}\Lambda_f[m_f(r,t) - m_f^{eq}(r,t)] + \delta t(\mathsf{I} - \tfrac{1}{2}\mathcal{Q}^{-1}\Lambda_f \mathcal{Q})G_i(r,t) \tag{6}$$

$$g_i(r+e_i\delta t, t+\delta t) = g_i(r,t) - \mathcal{Q}^{-1}\Lambda_g\left[m_g(r,t) - m_g^{eq}(r,t)\right] \tag{7}$$

where $f_i(r,t)$ and $g_i(r,t)$ represent the particle density distribution function and the order-parameter vectors respectively at location r and time t, $\Lambda_{\alpha(\alpha=f,g)}$ is the diagonal relaxation matrix, I is the identity matrix, and $\mathcal{Q}$ is a $q \times q$ matrix, which linearly transforms the distribution functions of f_i and g_i to the velocity moments m_f and m_g, respectively. In the work of Niu et al., more details about the LBM formulation are provided.[59]

In LBM, the diffuse interface approach is used to model multiphase flows. The main advantage of this approach is that the motion of the multiphase interface does not need to be explicitly tracked, and it is therefore very convenient for solving complex geometric problems. In this work, the phase and the interface are distinguished according to the value of φ in Equation (5) as follows:
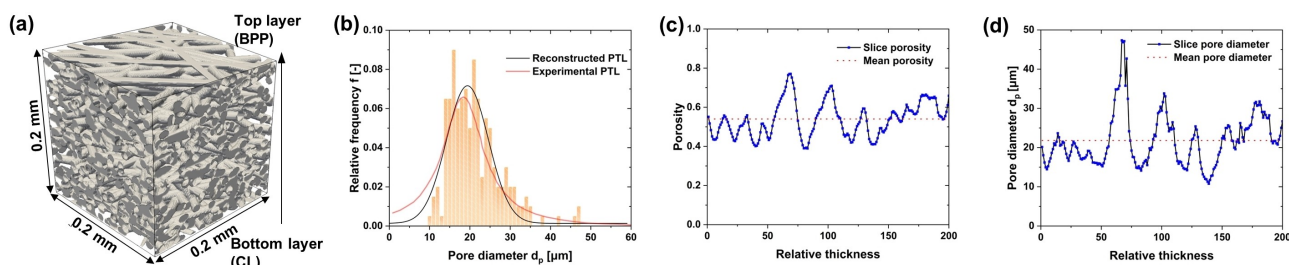
Figure 3. a) 3-D rendering of the reconstructed PTL, whereas all rendered PTLs within this work are chosen to have an edge length of 200 μm (or 0.2 mm as indicated here). b) The PSD; c) local porosity and d) local pore diameter along the through-plane direction for the herein reconstructed PTL.

$$\varphi > 0.7 \rightarrow \text{Liquid};\qquad(8)$$

$$-0.7 \leq \varphi < 0 \lor 0 < \varphi \leq 0.7 \rightarrow \text{Interface};\qquad(9)$$

$$\varphi < -0.7 \rightarrow \text{Gas}.\qquad(10)$$

To simulate the propagation of oxygen into the water-rich PTL, a single-lattice thick oxygen field was initialized next to the domain inlet, and the entire interior of the PTL was initialized with liquid water, as shown in Figure 1b. So, in the LBM simulation, a domain size of 200×201×200 μm³ (200×200×200 μm³ of the PTL structure and 200×1×200 μm³ of initial oxygen) was selected. A pressure gradient factor of 1.7 was applied to the inlet and outlet side to drive the oxygen into the PTL, and periodic boundary conditions were applied to the other boundaries. Besides, the non-compressible, isothermal, two-phase model was applied, and gravity and liquid films were neglected. The contact angle of Ti fibers was set to 45° (i.e., hydrophilic character) and the surface tension was set to 0.0625 N/m. Assuming a temperature of 298.15 K,[51] the density of water and oxygen was set to 997.05 kg/m³ and 1.14 kg/m³, respectively.

Simulation Workflow

The conducted studies involved the following workflow:
1. Reconstruction of PTLs via MATLAB;
2. Simulation of mass transport within the PTLs via LBM;
3. Post-processing through ParaView.

Specifically, the reconstruction of the PTL with target properties was first implemented in MATLAB and the numeric matrix information representing this PTL was derived. Subsequently, this matrix file was transferred to the LBM algorithm written in FORTRAN language, and then was identified and simulated. Finally, the simulation result files were exported to ParaView for post-processing to obtain the oxygen/water distributions. All LBM simulations were conducted on the Phoenix Cluster of the TU Braunschweig. Four compute nodes were applied in each case, each configured with two CPU INTEL Xeon E5-2640v4 and 64GB DDR4-2400 RAM. It took approximately six hours to complete 150,000 simulation steps for each case.

Results and Discussion

Validation and Analysis

In this section, the reconstruction of the PTL structures is validated, as conducted in Ref. [10]. In the stochastic reconstruction algorithm, the fiber diameter was set to 11.0 μm and the porosity to 54.0%. Fibers were stacked on the in-plane, and the overlapping of fibers allowed for accumulation.[60] The final 3-D rendering of the PTL structure reconstructed by the numerical stochastic method is shown in Figure 3a with a domain size of 200×200×200 μm³. Prior to the validation, the effect of PTL domain size (also the mesh-convergence) was tested, showing that spatial resolution is sufficiently fine. In addition, simulations for PTLs with the same morphological features but different internal structures indicate similar oxygen saturation profiles, demonstrating the reliability of subsequent results. For more details, please refer to the Figure S1 in the Supporting Information.

As shown in Table 1, the porosity, fiber diameter, and mean pore diameter of the reconstructed PTL agree well with the experimental measurement mentioned in literature. In addition to the basic structural parameters of the PTL, the PSD of porous structures also plays a pivotal role in mass transport. Figure 3b shows that the PSD curves are very similar. The small deviation in the PSD is attributed to the highly stochastic nature of PTL fabrication/reconstruction. We show that this deviation makes negligible contribution to the overall oxygen saturation profile (cf. Figure S1, Supporting Information). Moreover, it is acceptable in the observed range of porosity/fiber radius/anisotropy parameter in this work.

Besides, Figure 3c,d show the local porosity and pore diameter distribution along the through-plane direction of the

Table 1. Comparison of structural features between the reconstructed and experimental PTL.

PTLs	Porosity [%]	Fiber diameter [μm]	Mean pore diameter [μm]
Reconstructed PTL	54.0	11.0	21.8
Experimental PTL	55.0	11.0	20.6
Relative deviation	1.8%	0.0%	5.8%

ChemPhysChem

Research Article
doi.org/10.1002/cphc.202300197

Chemistry Europe
European Chemical
Societies Publishing

reconstructed PTL respectively. In the stochastic reconstruction algorithm, the fibers that make up the PTL structure were assumed to be long-straight cylindrical with a fixed and identical radius, resulting in greatly anisotropic fiber distributions and orientations in order to meet the target porosity, which in turn leads to a fluctuating local porosity and pore size distribution. This difference is also quite severe between sintered titanium powder-based PTLs and titanium felt-based PTLs,[9,10,20] in which sintered titanium powder-based PTLs have a relatively uniform porosity distribution.

After verifying the validity of the PTL stochastic reconstruction method in this work, the LBM was implemented to obtain the two-phase (gaseous oxygen/liquid water) distribution inside the reconstructed PTL to evaluate the impact of the PTL structural parameters on the transport of oxygen.

In the simulation, the oxygen propagation over time in the PTL is represented by the numerical results at different simulation steps, which means that the simulation step approximately represents the evolution of time. Figure 4 shows the oxygen propagation pattern in the PTL at the 100,000th simulation step. In Figure 4, blue color represents oxygen, red color represents liquid water, and gray color represents solid fibers. At the 100,000th simulation step, oxygen has been transported from the bottom to the top of the PTL, and the PTL is partially flooded with oxygen. Some oxygen has reached the outlet side of the PTL. The path through which the oxygen flows from the CL to the BPP is usually termed as a pathway. Figure 4 shows that several pathways are established for oxygen to escape from the PTL, which implies an efficient removal of oxygen from different locations. This finding is consistent with 2-D observations in previous works.[31,46]

To further observe how oxygen is transported out of the PTL, a series of 2-D and 3-D snapshots of the oxygen propagation process at different simulation steps (the 10,000th, 30,000th, 50,000th, 70,000th, 100,000th simulation step) are shown in Figure 5a,b, where the yellow color represents oxygen, and the aquamarine represents liquid water. Oxygen moves from the inlet to the outlet within 70,000 simulation steps, and in the subsequent process, the liquid water is further displaced and more pathways are developed. When exploring the formation of oxygen pathways, it should be emphasized that the development rates of these pathways are eminently different, which is ascribed to the local capillary resistance and pore structure of the pathway. The solid line in Figure 5c shows the maximum propagation distance of oxygen as iterations evolve, where the dashed lines represent the oxygen propagation rate at every 10,000 simulation steps. It is observed that the rate of oxygen removal is significantly faster at the 0–10,000th simulation steps and the 50,000th–60,000th simulation steps, which corresponds to the 0–60 and 150–190 y-positions of the PTL relative thickness, respectively. Figure 3c,d show that the porosity and pore diameter are relatively small but uniform at these positions, while the porosity and pore diameter change more drastically at the middle position of the PTL, which may be the reason for the slower propagation of oxygen into this location.
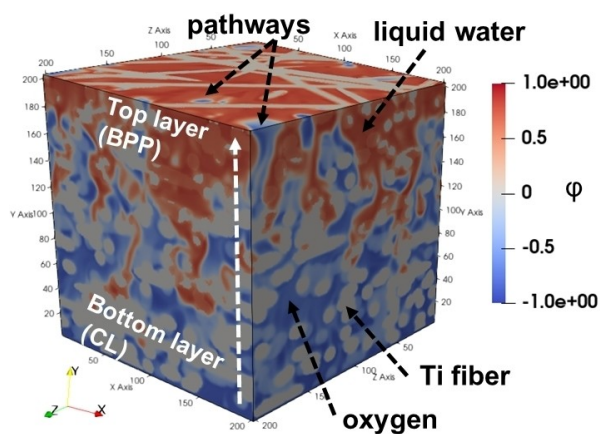

Figure 4. The oxygen propagation pattern in the computational domain at the 100,000th simulation step. The blue color represents oxygen, the red color represents liquid water, and the gray color represents solid fibers. The subsequent figures show oxygen and liquid water in these colors unless otherwise indicated.
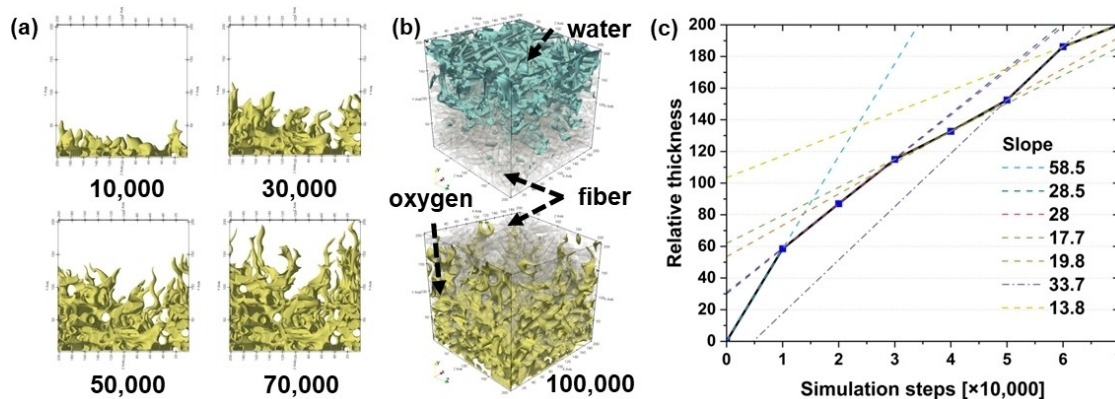

Figure 5. a) Propagation processes of oxygen inside the PTL as the iterative simulation evolves, b) distributions of liquid water (top) and oxygen (bottom), with solid structures shown transparent at the 100,000th simulation step, and c) the maximum propagation distance of oxygen at different simulation steps. The colored dashed lines represent the oxygen propagation rate at every 10,000 simulation steps. In (a) and (b), the yellow color represents oxygen, and the aquamarine represents liquid water.

A sequence of snapshots for oxygen propagation patterns at discrete *x*-locations at different simulation steps (the 30,000[th], 50,000[th], 70,000[th], 100,000[th] simulation step) is shown in Figure 6a. The LBM simulations demonstrate an excellent ability to capture the two phase distributions, mainly due to the ability to adapt to the physics of pore-scale events such as capillary value effects (CVE) and Haines jumps.[31] In the above observations, it was found that oxygen propagation is faster at the inlet and outlet sides of the PTL due to the more uniform porosity and pore size distribution, while it is slower at the middle position of the PTL. Figure 6a illustrates that at the *x*-position of 100–140, there is particularly low amounts of oxygen entering in the early simulation, and as the iteration progresses, the oxygen distribution at this location is still low and the propagation develops slowly. However, concentrated oxygen distribution and rapid development of propagation can be observed at outer locations of the PTL, which can be observed more intuitively and clearly from the oxygen propagation patterns at discrete *y*-locations at the 100,000[th] simulation step in Figure 6b. These observations suggest that the outer structure of the reconstructed PTL facilitates the rapid propagation and removal of oxygen, while the inner structural properties will lead to slow passage of oxygen or even blockage. This phenomenon can be explained as follows. Figure 6b and Figure 5b demonstrate the oxygen propagation patterns for different in-plane locations and the oxygen/liquid water distribution at the 100,000[th] simulation step, respectively. It can be observed in the slice of *y* = 20 in Figure 6b that the fibers crisscross on the inlet side of the PTL, resulting in the intermediate region being almost completely occupied by the solid structure, which makes it difficult for oxygen to enter

these small pores[44] at the start of the simulation. Moreover, although the pore space appears to be wider at a position further down, the oxygen pathways have already formed at the periphery of the PTL, which means that there is less capillary resistance for oxygen to escape here.[32] So, the pore structure in the mid region of the PTL will hardly be fully utilized. As a result, it will be difficult for the oxygen to move away from this area.

In the real electrolysis application, this could imply that such a PTL would not be ideal to maintain the electrochemical reactions. The lack of transport of oxygen from the reaction sites of the catalyst layer to the outside would decrease the overall electrolysis cell performance. Therefore, when designing or using PTLs, it should be ensured as much as possible that the side close to the catalyst layer has appropriate porosity and pore structure, avoiding locally dense fibers, which may block the pathways of the gas.

So far, the feasibility of the reconstruction method in this work and the reliability of LBM in predicting oxygen propagation patterns in PTLs have been demonstrated and verified. In the following, the impact of the structural properties of the PTL, including the porosity, fiber radius, and anisotropy parameter, on mass transport will be analyzed and discussed.

Impact of the Porosity

Five PTLs with varied porosity from 0.44 to 0.84 were reconstructed as described before (see Figure 2c). Figure 7 shows the detailed spatial structural information corresponding to the five PTLs. Figure 7a shows that as the porosity increases,
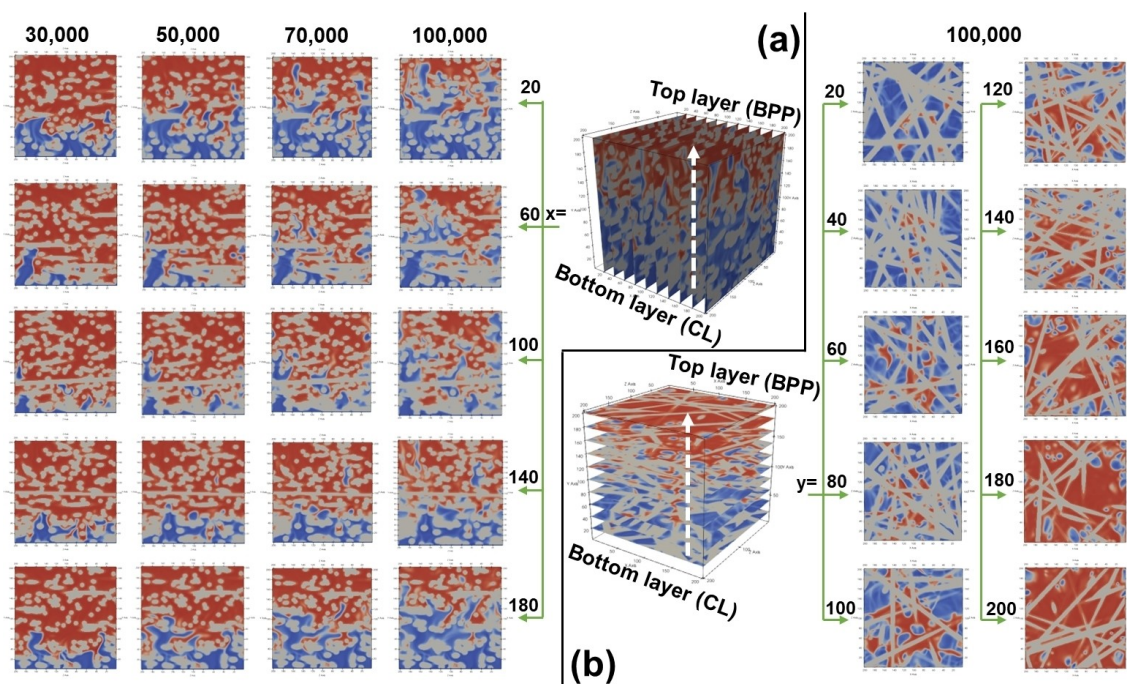

Figure 6. Oxygen propagation patterns at a) discrete *x*-locations (through-plane) at the 30,000[th], 50,000[th], 70,000[th], and 100,000[th] simulation step and b) discrete *y*-locations (in-plane) at the 100,000[th] simulation step.

ChemPhysChem

Research Article
doi.org/10.1002/cphc.202300197

Chemistry
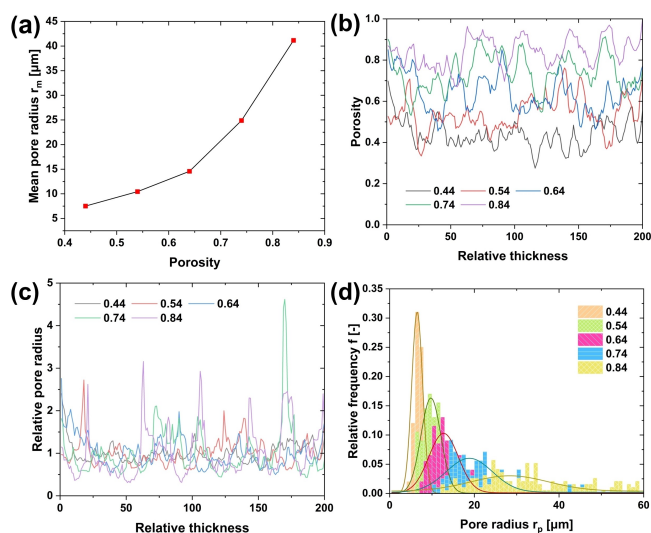**Europe**
European Chemical
Societies Publishing

Figure 7. a) The mean pore radius, b) local porosity distribution, c) local relative pore radius distribution along the through-plane direction, and d) the PSD of PTLs with different porosity (the five PTLs have a consistent fiber radius of 5.0 μm).

in the Validation and Analysis section. Likewise, Figure 7c depicts that the value of pore radius also fluctuates frequently along the through-plane direction, and a trend can be observed: As the porosity increases, the pore radius value fluctuates more frequently and in a greater amplitude, resulting in more varied local pore structural characteristics. Figure 7d indicates that the PTL with a low porosity features a more uniform pore size.

LBM simulations were implemented for the five reconstructed PTL structures. Figure 8a shows imbibition curves of oxygen into the pores of the PTLs with different porosity. After 150,000 simulation steps, the PTLs with the porosity of 0.84 and 0.74 have already reached full saturation, those with 0.64 are almost saturated, and those with 0.54 and 0.44 still need longer to reach full saturation with oxygen. At the same simulation step, the oxygen saturation is higher in the PTL structure with higher porosity. The PTL with a porosity of 0.44 takes 114,000 simulation steps to reach a saturation of 0.4, which is approximately two times and twelve times the simulation steps required for PTLs with a porosity of 0.54 or 0.84, respectively. All in all, these results reveal that more oxygen can be transported out of the PTL with higher porosity.

Figure 9 shows the LBM simulation results of PTLs with different porosity at the 20,000th simulation step. In the PTL with a higher porosity, oxygen not only invades faster, but also appears to reach more propagation pathways, especially in the early stage of propagation. In practical applications of PTLs, it is not only the rapid formation of oxygen propagation pathways that is required, but also the number of propagation pathways in the PTL is crucial as this will avoid localized oxygen blockages at the PTL-CL interface. For the lower-porosity PTL structures, the resistance experienced by oxygen to be transported out of the PTL is greater. While for the higher-porosity PTLs, this resistance is relatively small and the sparsely distributed Ti fibers lead to more possibilities for oxygen removal from the catalyst layer and the PTL. This fact ultimately leads to faster oxygen removal and more pathways in the higher-porosity PTL structures.
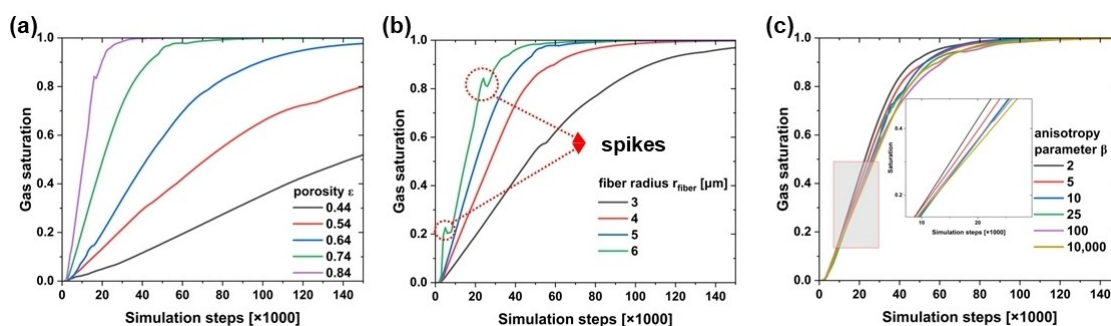
the pore size shifts to bigger values, which is consistent with experimental results.[9] Besides, the slope changes significantly. It is less steep for lower porosity region while it is much steeper for higher porosity region.

Upon further examination of the structural differences of the 3-D reconstructed PTLs with different porosity, the local porosity distribution, the local relative pore radius distribution along the through-plane direction, and the PSD of the five PTLs are shown in Figure 7 as well. The concept of relative pore radius r_{rel} is defined here to evaluate the magnitude of the pore size variation of the PTLs. It can be calculated as follows [Eq. (11)]:

$$r_{rel} = \frac{r_p}{r_m} \qquad (11)$$

where r_p is the local pore radius and r_m is the mean pore radius. Figure 7b shows that the local porosity of the five PTLs along the through-plane direction fluctuates around their respective target porosity, and the maximum fluctuation range is $-0.21\sim$ $+0.25$. The reason for porosity fluctuation has been explained

Figure 8. The oxygen saturation as the iteration evolves for PTLs with a) different porosity, b) different fiber radii, and c) different anisotropy parameters.
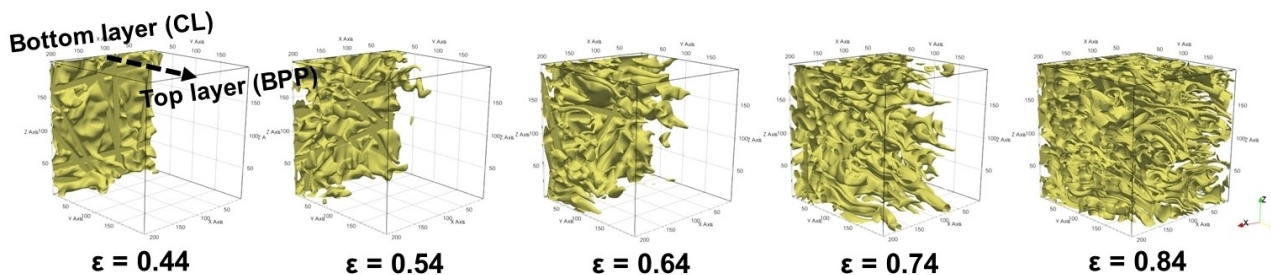
Figure 9. Oxygen distributions at the 20,000th simulation step of PTLs with different porosity.

Impact of Fiber Radius

Four reconstructed PTLs with the same porosity of 0.74 and different fiber radii (3.0 μm, 4.0 μm, 5.0 μm, and 6.0 μm, respectively) are shown in Figure 2d. The mean pore radii of the four PTLs are also calculated and shown in Figure S2 (cf. Supporting Information), which are 12.3 μm, 17.8 μm, 23.5 μm, and 26.3 μm, respectively. For PTL structures with the same porosity and domain size goes that the larger the radius of the fibers constituting the porous structure, the larger the mean pore size of the PTL. Figure S2 also demonstrates the local porosity distribution, local relative pore radius distribution along the through-plane direction, and the PSD of the four reconstructed PTLs respectively. Although the fiber radii differ from each other, for PTL structures with the same porosity, the local porosity variation along the through-plane direction is almost identical. On the contrary, it can be observed in Figure S2 that the PSD of the PTL with a smaller fiber radius is relatively sharper and denser, which indicates a more uniform pore size, and as the fiber radius increases, the fluctuation range of the pore size value becomes wider. Table 2 lists the mean and extreme values of the pore size of the PTLs with different fiber radius values.

Again, LBM simulations were performed with the four reconstructed PTLs, and the oxygen saturation is obtained as shown in Figure 8b. Except for the PTL with a fiber radius of 3.0 μm that has not reached full saturation after 150,000 simulation steps, all PTLs have reached full saturation. It appears that the larger the fiber radius value, the faster the saturation. These four PTL structures comprise the same porosity distributions, and the only variable is the pore size resulting from varied fiber radii. It can be concluded that the oxygen removal rate from the PTL is proportional to the fiber radius.

In addition, an interesting phenomenon is found in the oxygen saturation curve of the PTL with a fiber radius of 6.0 μm in Figure 8b: Two "spikes" appear during the development of the oxygen saturation curve. Inspection of the oxygen propagation process revealed that oxygen has already been transported to the outlet side of the PTL in less than 10,000 simulation steps, as shown in Figure 10. Furthermore, it can be observed from the local relative pore radius distribution in Figure S2 that the pore size of the PTL with a fiber radius of 6.0 μm increases dramatically at the outlet side of the PTL, implying that oxygen transported to the pores at this location requires a pressurization and penetration process.[46] During the pressurization, oxygen accumulates in the pores and the oxygen saturation rises; once the condition for "penetration" is reached, oxygen is rapidly transported out of the PTL, causing a brief drop in oxygen saturation, and resulting in a "spike" phenomenon.

From the 3-D PTL cubic structure, a 2-D slice was made along the volume diagonal to obtain the 2-D oxygen propagation patterns. The effect of the pore distribution on the
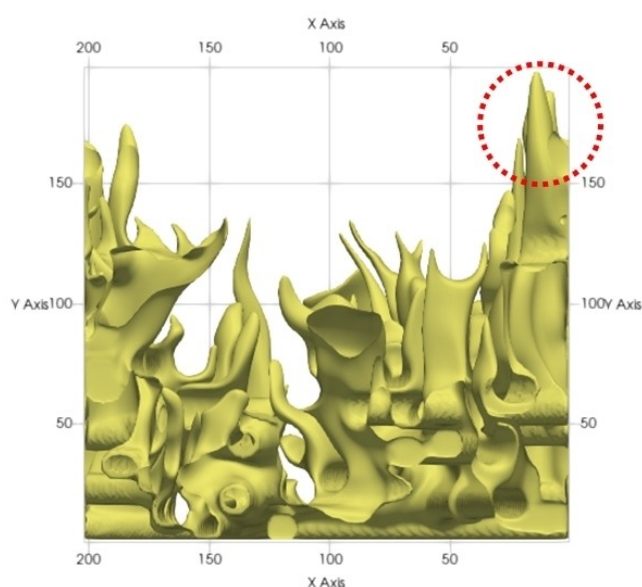
Table 2. The pore sizes of PTLs with the same porosity of 0.74 and different fiber radii.

Fiber radius [μm]	Mean pore radius [μm]	Max. pore radius [μm]	Min. pore radius [μm]
3.0	12.3	26.6	6.8
4.0	17.8	47.4	8.6
5.0	23.5	62.9	10.0
6.0	26.3	71.5	11.8

Figure 10. Oxygen distribution at the 10,000th simulation step of the PTL with a fiber radius of 6.0 μm. The circle indicates oxygen clusters reaching the outlet.
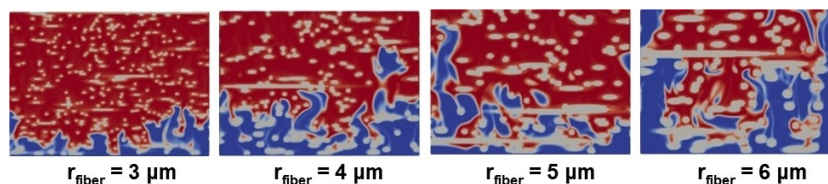
ChemPhysChem

Research Article
doi.org/10.1002/cphc.202300197

Chemistry Europe
European Chemical
Societies Publishing

Figure 11. 2-D slices of oxygen propagation patterns at the 20,000th simulation step of PTLs with different fiber radii.
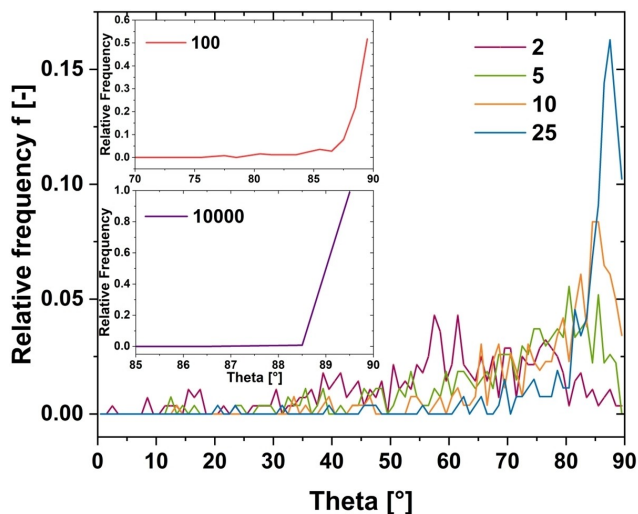

Figure 13. The θ distributions of PTLs with different β values.

Figure 12 demonstrates the evolutions of oxygen propagation patterns for PTLs with a fiber radius of 3.0 μm and 4.0 μm. The rightmost plots in Figure 12 show the pore structure, where black represents solid fibers and gray represents pore space. With the iteration evolution, oxygen continuously permeates the PTL pore structure, and several local 2-D oxygen propagation pathways can thus be generalized, as shown by the colored solid lines in Figure 12 (right side). It is indicated that the propagation pathways consist of a series of sparsely distributed pores. The pathway indicated in red is almost the fastest to break through, which means the least resistance is required for the removal of oxygen here. When an oxygen propagation pathway is established, the formation of a new pathway needs to overcome greater resistance than it takes to follow the established pathway.[32] In addition to this finding, the propagation pathways in the PTL with a fiber radius of 4.0 μm are formed much earlier than that in the PTL with a fiber radius of 3.0 μm.

transport of oxygen is illustrated by taking the simulation results at the 20,000th simulation step as an example (cf. Figure 11). Although the PTL structure with a higher mean pore size has a significant advantage in the removal of oxygen from the porous structure, it can still be observed that the middle location of the PTL structure with a fiber radius of 6.0 μm is blocked for the transport of oxygen, which is mainly caused by unreasonable pore distribution in certain locations. Therefore, it should be noted that the pore distribution in the PTL has a significant impact on mass transport, and a reasonable pore distribution will be more beneficial to the supply of water from the flow channel to the catalyst layer and the removal of oxygen from the catalyst layer to the flow channel.

Impact of Anisotropy Parameter

A novel angled gas diffusion layer capable of enhancing the performance of PEMFC was proposed in the work of Zhu et al.[61] To the best of our knowledge, the herein presented work is the first study on the impact of fiber orientation of the felt PTL on the mass transport within PEMECs. Six PTLs sharing a fixed porosity of 0.74 and a fiber radius of 4.0 μm with different fiber orientations were reconstructed to explore the impact of structural anisotropy on oxygen removal from PTLs, as shown in Figure 2e. Figure 13 demonstrates the distributions of polar angle θ values describing the angle between fiber orientation and through-plane of PTLs with different β values. As the β value approaches the value of one, more fibers tend to
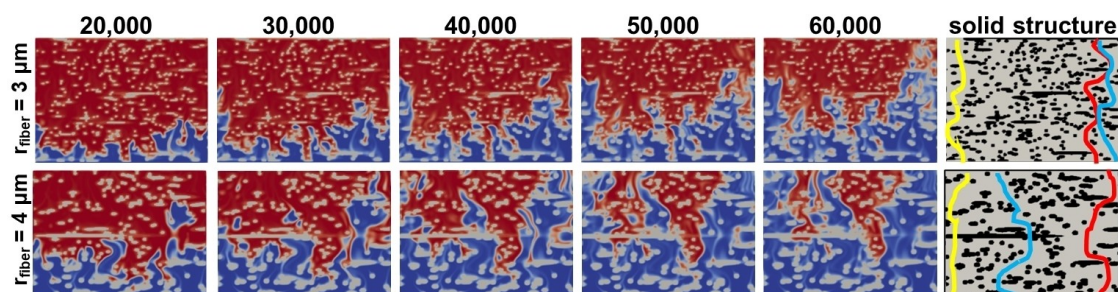

Figure 12. 2-D slices of oxygen propagation patterns of PTLs with a fiber radius of 3.0 μm and 4.0 μm as the iteration evolves.

ChemPhysChem

Research Article
doi.org/10.1002/cphc.202300197

Chemistry
Europe
European Chemical
Societies Publishing

be at a 45° (also 135°) angle to the through-plane, resulting in a uniformly distributed structure. When the β value is 10,000, all fibers are oriented at 90° direction, which indicates that the fibers will be stacked horizontally.

The β value affects the internal structural characteristics of the PTL by changing the orientation of the fibers. Figure S3 (cf. Supporting Information) plots the mean pore radii and the internal details of these reconstructed PTLs with different β values. Overall, compared to porosity and fiber radius, the anisotropy parameter does not affect the mean pore size very strongly. When the PTL structure has a small β value, it tends to be uniform in all directions, the mean pore radius is smaller, and the pore size distribution becomes denser. The pore radius of the PTL with a β value of 2 ranges from 10.8 μm to 18.6 μm, while that with a β value of 10,000 ranges from 8.6 μm to 47.4 μm. In addition to the mean pore radius and pore size distribution, the local porosity distribution and local relative pore radius distribution of PTL structures with different anisotropy parameters also differ from each other. In addition, a correlation between the local porosity/pore radius distribution along the TP direction and PSD can be derived from Figure S3. The local porosity/pore radius fluctuates less drastically, if the PSD exhibits steeper curves, i.e., more homogenous pore sizes.

After elucidating the impact of the anisotropy parameter on the internal structural characteristics of PTLs, LBM-based simulations were performed for these PTLs. Oxygen saturation results with iteration evolution are obtained as shown in Figure 8 (c). All PTLs eventually reach full saturation at about the same simulation step, but before reaching full saturation, PTLs with smaller β values are able to reach the same saturation level earlier than PTLs with larger β values. It is particularly worth noting that although PTLs with larger β values have relatively larger mean pore radii, they are not more favorable regarding the removal of oxygen here.

Although the anisotropy parameter only has a slight impact on the oxygen saturation for the PTLs with a relatively higher porosity, the PTL with a small β value can still achieve a local oxygen propagation pathway faster, as shown in Figure 14a. In addition, the fibers with small β values are not parallel to the interface between the PTL and CL, but at a certain angle. The oxygen generated by the electrochemical reaction on the CL can enter the nearby pore space in time and escape through its local pathway, avoiding the stay at the reaction site and facilitating the supply of water and the progress of the local electrochemical reaction. Figure 14b shows that a PTL with a smaller β value is beneficial to the convergence of oxygen, and because there is no obstruction of transverse fibers, oxygen bubbles can pass through various positions in the in-plane. On the contrary, a PTL with a larger β value may cause the local pores in the in-plane to be unable to be utilized for oxygen removal due to the dense crisscross of fibers.

Optimal Oxygen Transport in PTLs

In previous studies,[20,29,44,51] spatially gradient-porosity PTLs were proposed to trade off ohmic losses and mass transport losses, which further enhanced the performance of PEM electrolyzers. Although the low-to-high porosity PTL configuration from CL to BPP has been reported to enhance the performance of PEM electrolyzers, the mass transport behavior within the PTL has not been investigated in detail.

Herein, we analyze first two configurations to elucidate the impact of the directionality of the porosity gradient (low-to-high and high-to-low porosity). The PTL configuration for the low porosity region adjacent to the CL and high porosity region close to the BPP is denoted as "LtoH", and vice versa as "HtoL". Besides, another PTL structure with the same porosity gradient as "LtoH" (0.44–0.74 from the CL to the BPP) but with a different fiber radius and orientation was reconstructed and noted as "LtoH_opt", which is expected to enhance the mass transport behavior. These graded PTLs were obtained by merging two layers of PTLs of the same thickness with different porosity into one layer, as shown in Figure 15a. The differences in porosity gradient and fiber parameters of the three graded PTLs are shown in Figure 15b.

Figure 15c and Figure 16 demonstrate the gas saturation profiles and oxygen propagation processes obtained via LBM simulations. The PTLs "LtoH" and "LtoH_opt" exhibit a completely different trend compared to "HtoL" in terms of gas saturation profiles, as shown in Figure 15c. The PTL "HtoL" shows significantly higher gas saturation in the high-porosity region near the CL and extremely low gas saturation in the low-porosity region near the BPP. Along the through-plane direction, the gas saturation of "HtoL" becomes progressively lower, with an abrupt drop in saturation at the corresponding position in the transition from the high to the low porosity region. This phenomenon can be attributed to the difference in the resistance to gas removal caused by the pore structures. Figure 16a indicates that during the gas propagation process, oxygen first accumulates preferentially in the larger pores in the high porosity region, while the sudden reduction in porosity results in smaller pores and thus displaying greater resistance to gas removal[44] and slower propagation rates. This behavior will eventually result in the oxygen near the CL side not being
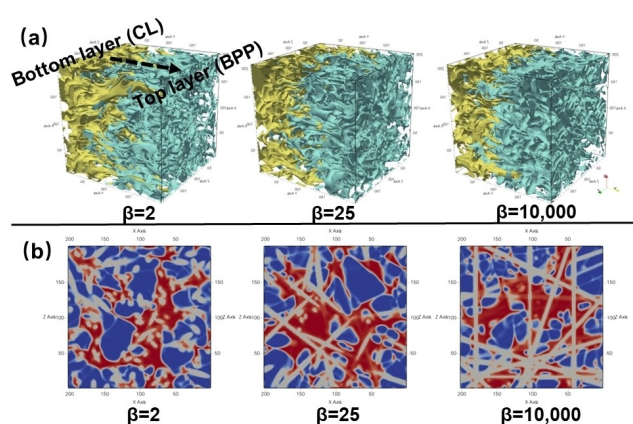

Figure 14. a) Oxygen (yellow) and water (aquamarine) distributions and b) 2-D slices of oxygen propagation patterns at $y = 50$ μm in-plane at the 20,000th simulation step of PTLs with different β values.

ChemPhysChem

Research Article
doi.org/10.1002/cphc.202300197

**Chemistry
Europe**
European Chemical
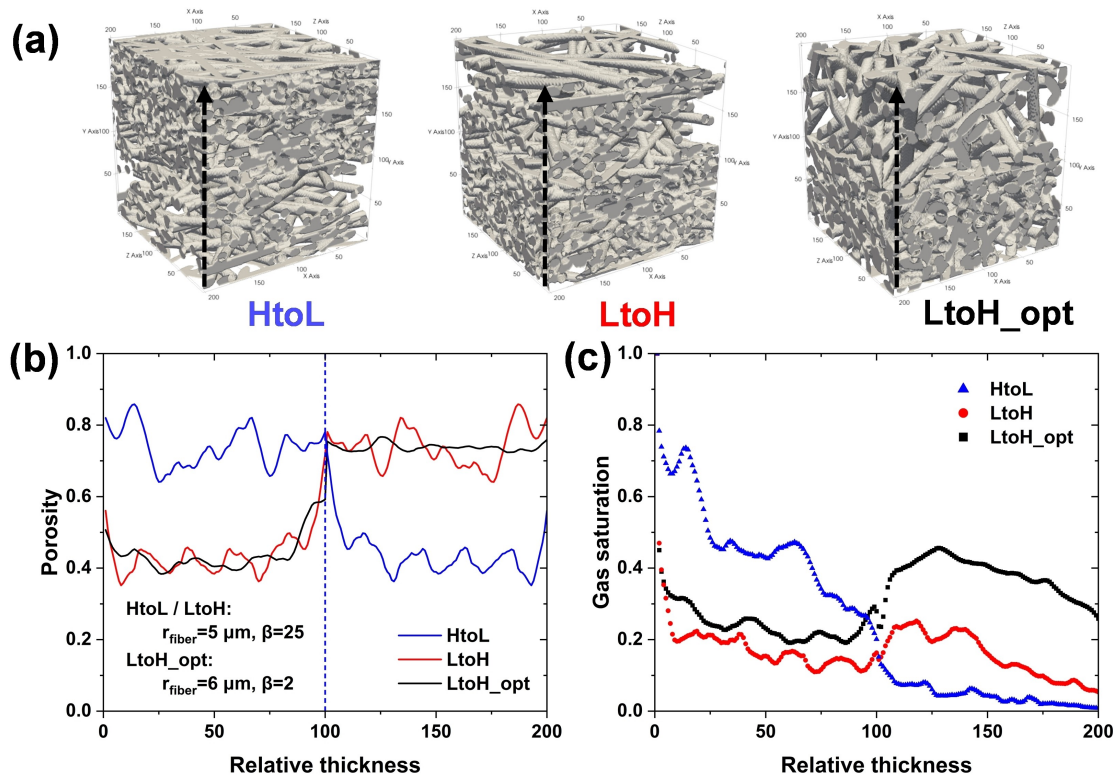Societies Publishing

Figure 15. a) 3-D renderings of the reconstructed graded PTLs. b) The structural features of the three graded PTLs. c) The gas saturation profiles at the 150,000[th] simulation step obtained via LBM simulations for different graded PTLs.
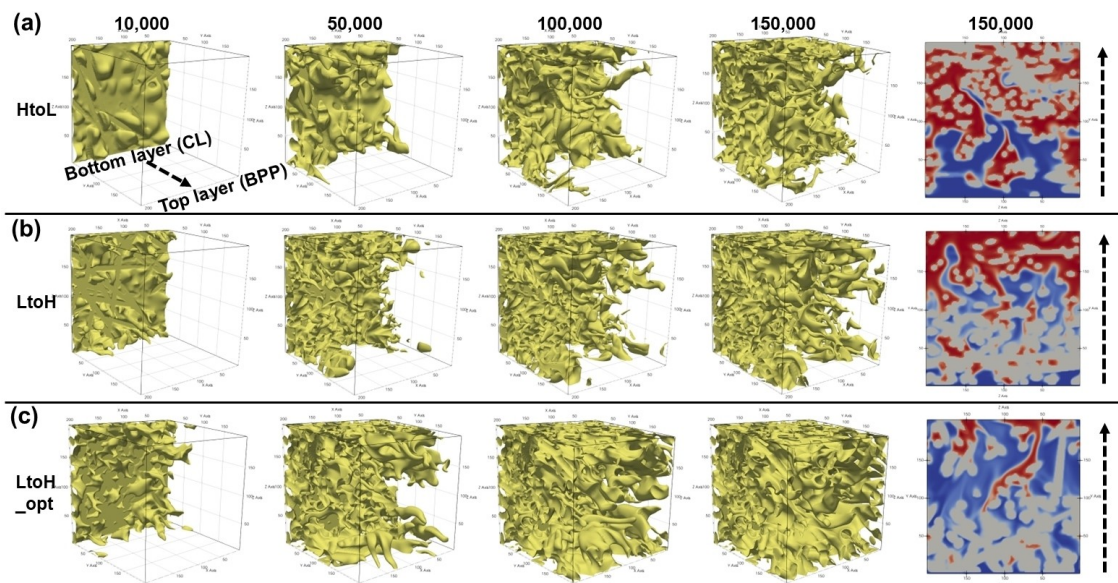

Figure 16. The oxygen propagation processes of the graded PTLs: a) HtoL, b) LtoH and c) LtoH_opt.

removed in time, impeding the supply of reactant water and thus leading to both mass transport limitations and membrane dehydration in the context of electrolyzer operation.[62–64] In contrast, PTL configurations ranging from low to high porosity provide relatively satisfactory results. Both "LtoH" and "LtoH_opt" show a strong ability to transport the oxygen out of the

PTLs (cf. Figure 16b,c). The transition in porosity from low to high allows oxygen to be transported away from the CL and to accumulate in the pores close to the BPP and subsequently flow out quickly. The impact of the directionality of the porosity gradient on mass transport behavior is tentatively demonstrated, with a low to high porosity from the CL to BPP

ChemPhysChem

Research Article
doi.org/10.1002/cphc.202300197

**Chemistry
Europe**
European Chemical
Societies Publishing

facilitating oxygen removal and water supply. More promisingly, the optimal performance seems to be obtained from PTL "LtoH_opt" by tailoring the fiber properties of PTLs with the same porosity gradient. As can be seen from the red and black dotted lines in Figure 15c, at each position along the TP direction, the "LtoH_opt" exhibits a higher oxygen saturation relative to the "LtoH", which indicates that the structure is more conducive to the rapid propagation of oxygen into the pore spaces and the subsequent rapid removal. Comparing the oxygen propagation processes in Figure 16b,c, the "LtoH_opt" exhibits faster propagation and more propagation pathways at the same simulation step, which indicates that better oxygen removal can be expected for the operation of an electrolyzer with this PTL configuration.

For future practical implementation, we offer some ideas for reproducing this structure. The main difference from conventional felt PTLs is that we propose to adjust the fiber orientation. Thus, techniques such as 3D printing could be an option to manufacture separately the top and bottom layers with individual porosity and fiber characteristics of the PTL. The fibers should be oriented at an angle of 30–45° to the in plane. Subsequently, the two layers are merged into a complete PTL by compression or hot pressing for the electrolyzer assembly.

Conclusions

In this work, a stochastic numerical reconstruction method for titanium felt-based PTLs of PEMEC was applied to reconstruct PTLs with customized structural properties. These reconstructed PTLs were simulated by LBM to obtain oxygen propagation patterns and two-phase distributions. The results were used to assess the impact of PTL structures on the transport of oxygen and then to tailor a customized graded PTL with optimal mass transport performance. Structural characteristics from reported experimental PTLs in the published literature were used to verify the validity of the method and the results are in good agreement. The LBM results show that: 1) a higher porosity of PTLs favors the removal of oxygen; 2) the removal rate of oxygen is proportional to the fiber radius of PTLs; 3) PTLs with an angle between the fiber and the interface of the PTL and CL facilitate the removal of oxygen. Besides, relatively uniform porosity and sharp pore size distribution favor the rapid formation of oxygen propagation pathways and the sides of PTLs near the CL should avoid too dense fiber crossing, which should be ensured maximally in the design and manufacture of all PTLs. More importantly, the low-to-high porosity PTL configuration from the CL to BPP is able to enhance the transport of oxygen. This can be the primary options for weighing mass transport and interfacial contact. The graded PTLs obtained by tailoring the fiber properties allow for optimal mass transport performance. For the first time, the impact of the PTL anisotropy on mass transport behavior was investigated and the mass transport performance of a graded PTL was optimized by parametrically tailoring and customizing the fiber properties. From this work, a systematic approach for exploring the impact of PTL structural properties on the oxygen transport

within the PTL of electrolyzers and a few PTL design suggestions are obtained. This approach and the conclusions provide effective insights into designing PTL materials to enhance the performance of PEM electrolyzers for future applications.

Conflict of Interests

The authors declare no conflict of interest.

Data Availability Statement

The data that support the findings of this study are available from the corresponding author upon reasonable request.

[1] The Future of Hydrogen, International Energy Agency, Paris, France, **2019**.
[2] A. Hodges, A. L. Hoang, G. Tsekouras, K. Wagner, C. Y. Lee, G. F. Swiegers, G. G. Wallace, *Nat. Commun.* **2022**, *13*, 1304.
[3] S. Shiva Kumar, V. Himabindu, *Mater. Sci. Energy Technol.* **2019**, *2*, 442–454.
[4] D. S. Falcão, A. M. F. R. Pinto, *J. Cleaner Prod.* **2020**, *261*.
[5] D. Bessarabov, H. Wang, H. Li, N. Zhao, *PEM electrolysis for hydrogen production: principles and applications*, CRC press, **2016**.
[6] M. Carmo, D. L. Fritz, J. Mergel, D. Stolten, *Int. J. Hydrogen Energy.* **2013**, *38*, 4901–4934.
[7] S. D. Greenway, E. B. Fox, A. A. Ekechukwu, *Int. J. Hydrogen Energy.* **2009**, *34*, 6603–6608.
[8] M. Ni, M. K. H. Leung, D. Y. C. Leung, *Energy Convers. Manage.* **2008**, *49*, 2748–2756.
[9] L. Zielke, A. Fallisch, N. Paust, R. Zengerle, S. Thiele, *RSC Adv.* **2014**, *4*, 58888–58894.
[10] T. Schuler, R. De Bruycker, T. J. Schmidt, F. N. Büchi, *J. Electrochem. Soc.* **2019**, *166*, F270-F281.
[11] X. Huang, W. Zhou, D. Deng, *Materials (Basel).* **2021**, *14*.
[12] M. Suermann, K. Takanohashi, A. Lamibrac, T. J. Schmidt, F. N. Büchi, *J. Electrochem. Soc.* **2017**, *164*, F973-F980.
[13] S. Jung, M. Sabharwal, A. Jarauta, F. Wei, M. Gingras, J. Gostick, M. Secanell, *J. Electrochem. Soc.* **2021**, *168*.

ChemPhysChem

Research Article
doi.org/10.1002/cphc.202300197

Chemistry
Europe

European Chemical
Societies Publishing

[14] V. Baglio, R. Ornelas, F. Matteucci, F. Martina, G. Ciccarella, I. Zama, L. G. Arriaga, V. Antonucci, A. S. Aricò, *Fuel Cells.* **2009**, *9*, 247–252.

[15] S. Siracusano, V. Baglio, N. Briguglio, G. Brunaccini, A. Di Blasi, A. Stassi, R. Ornelas, E. Trifoni, V. Antonucci, A. S. Aricò, *Int. J. Hydrogen Energy.* **2012**, *37*, 1939–1946.

[16] C. H. Lee, R. Banerjee, F. Arbabi, J. Hinebaugh, A. Bazylak, in *ASME 2016 14th International Conference on Nanochannels, Microchannels, and Minichannels collocated with the ASME 2016 Heat Transfer Summer Conference and the ASME 2016 Fluids Engineering Division Summer Meeting, Vol. ASME 2016 14th International Conference on Nanochannels, Microchannels, and Minichannels*, **2016**.

[17] J. Mo, Z. Kang, G. Yang, S. T. Retterer, D. A. Cullen, T. J. Toops, J. B. Green, F.-Y. Zhang, *Appl. Energy.* **2016**, *177*, 817–822.

[18] C. M. Hwang, M. Ishida, H. Ito, T. Maeda, A. Nakano, A. Kato, T. Yoshida, *J. Power Sources.* **2012**, *202*, 108–113.

[19] C. H. Lee, J. K. Lee, B. Zhao, K. F. Fahy, A. Bazylak, *J. Electrochem. Soc.* **2020**, *167*.

[20] P. Lettenmeier, S. Kolb, N. Sata, A. Fallisch, L. Zielke, S. Thiele, A. S. Gago, K. A. Friedrich, *Energy Environ. Sci.* **2017**, *10*, 2521–2533.

[21] T. Schuler, T. J. Schmidt, F. N. Büchi, *J. Electrochem. Soc.* **2019**, *166*, F555-F565.

[22] C. Lee, B. Zhao, R. Abouatallah, R. Wang, A. Bazylak, *Phys. Rev. Appl.* **2019**, *11*.

[23] F. Arbabi, A. Kalantarian, R. Abouatallah, R. Wang, J. S. Wallace, A. Bazylak, *J. Power Sources.* **2014**, *258*, 142–149.

[24] O. F. Selamet, U. Pasaogullari, D. Spernjak, D. S. Hussey, D. L. Jacobson, M. D. Mat, *Int. J. Hydrogen Energy.* **2013**, *38*, 5823–5835.

[25] O. Panchenko, E. Borgardt, W. Zwaygardt, F. J. Hackemüller, M. Bram, N. Kardjilov, T. Arlt, I. Manke, M. Müller, D. Stolten, W. Lehnert, *J. Power Sources.* **2018**, *390*, 108–115.

[26] A. Nouri-Khorasani, E. Tabu Ojong, T. Smolinka, D. P. Wilkinson, *Int. J. Hydrogen Energy.* **2017**, *42*, 28665–28680.

[27] S. A. Grigoriev, P. Millet, S. A. Volobuev, V. N. Fateev, *Int. J. Hydrogen Energy.* **2009**, *34*, 4968–4973.

[28] Z. Kang, S. Yu, G. Yang, Y. Li, G. Bender, B. S. Pivovar, J. B. Green, F.-Y. Zhang, *Electrochim. Acta.* **2019**, *316*, 43–51.

[29] J. Parra-Restrepo, R. Bligny, J. Dillet, S. Didierjean, D. Stemmelen, C. Moyne, A. Degiovanni, G. Maranzana, *Int. J. Hydrogen Energy.* **2020**, *45*, 8094–8106.

[30] F. Arbabi, H. Montazeri, R. Abouatallah, R. Wang, A. Bazylak, *J. Electrochem. Soc.* **2016**, *163*, F3062-F3069.

[31] S. Paliwal, D. Panda, S. Bhaskaran, N. Vorhauer-Huget, E. Tsotsas, V. K. Surasani, *Int. J. Hydrogen Energy.* **2021**, *46*, 22747–22762.

[32] P. Satjaritanun, M. O'Brien, D. Kulkarni, S. Shimpalee, C. Capuano, K. E. Ayers, N. Danilovic, D. Y. Parkinson, I. V. Zenyuk, *iScience.* **2020**, *23*, 101783.

[33] P. J. Kim, C. Lee, J. K. Lee, K. F. Fahy, A. Bazylak, *ECS Trans.* **2019**, *92*, 787–799.

[34] K. Wang, C. Liao, W. Wang, Y. Xiao, X. Liu, Y. Zuo, *ACS Appl. Energ. Mater.* **2020**, *3*, 6752–6757.

[35] H. Ito, T. Maeda, A. Nakano, C. M. Hwang, M. Ishida, A. Kato, T. Yoshida, *Int. J. Hydrogen Energy.* **2012**, *37*, 7418–7428.

[36] J. K. Lee, A. Bazylak, *ECS Trans.* **2017**, *80*, 1097–1106.

[37] J. K. Lee, A. Bazylak, *ECS Trans.* **2019**, *92*, 801–820.

[38] F. Arbabi, PhD thesis, University of Toronto (Canada), **2017**.

[39] A. Nouri Khorasani, PhD thesis, University of British Columbia (Canada), **2019**.

[40] D. Borah, PhD thesis, Forschungszentrum Jülich GmbH (Germany), **2021**.

[41] M. van der Heijden, R. van Gorp, M. A. Sadeghi, J. Gostick, A. Forner-Cuenca, *J. Electrochem. Soc.* **2022**, *169*.

[42] R. van Gorp, M. van der Heijden, M. Amin Sadeghi, J. Gostick, A. Forner-Cuenca, *Chem. Eng. J.* **2023**, *455*.

[43] C. H. Lee, J. K. Lee, B. Zhao, K. F. Fahy, J. M. LaManna, E. Baltic, D. S. Hussey, D. L. Jacobson, V. P. Schulz, A. Bazylak, *J. Power Sources.* **2020**, *446*.

[44] J. K. Lee, C. Lee, K. F. Fahy, P. J. Kim, J. M. LaManna, E. Baltic, D. L. Jacobson, D. S. Hussey, S. Stiber, A. S. Gago, K. A. Friedrich, A. Bazylak, *Energy Convers. Manage.* **2020**, *226*.

[45] Y. Li, Z. Kang, J. Mo, G. Yang, S. Yu, D. A. Talley, B. Han, F.-Y. Zhang, *Int. J. Hydrogen Energy.* **2018**, *43*, 11223–11233.

[46] C. Lee, J. Hinebaugh, R. Banerjee, S. Chevalier, R. Abouatallah, R. Wang, A. Bazylak, *Int. J. Hydrogen Energy.* **2017**, *42*, 2724–2735.

[47] G. F. Swiegers, R. N. L. Terrett, G. Tsekouras, T. Tsuzuki, R. J. Pace, R. Stranger, *Sustain. Energy Fuels* **2021**, *5*, 1280–1310.

[48] H. Ito, T. Maeda, A. Nakano, A. Kato, T. Yoshida, *Electrochim. Acta.* **2013**, *100*, 242–248.

[49] S. Stiber, H. Balzer, A. Wierhake, F. J. Wirkert, J. Roth, U. Rost, M. Brodmann, J. K. Lee, A. Bazylak, W. Waiblinger, A. S. Gago, K. A. Friedrich, *Adv. Energy Mater.* **2021**, *11*.

[50] T. L. Doan, H. E. Lee, S. S. H. Shah, M. Kim, C. H. Kim, H. S. Cho, T. Kim, *Int. J. Energy Res.* **2021**, *45*, 14207–14220.

[51] S. Bhaskaran, D. Pandey, V. K. Surasani, E. Tsotsas, T. Vidakovic-Koch, N. Vorhauer-Huget, *Int. J. Hydrogen Energy.* **2022**, *47*, 31551–31565.

[52] C. M. Hwang, M. Ishida, H. Ito, T. Maeda, A. Nakano, Y. Hasegawa, N. Yokoi, A. Kato, T. Yoshida, *Int. J. Hydrogen Energy.* **2011**, *36*, 1740–1753.

[53] S. Simaafrookhteh, M. Shakeri, M. Baniassadi, A. A. Sahraei, *Fuel Cells.* **2018**, *18*, 160–172.

[54] S. Simaafrookhteh, R. Taherian, M. Shakeri, *J. Electrochem. Soc.* **2019**, *166*, F3287-F3299.

[55] H. Deng, Y. Hou, K. Jiao, *Int. J. Heat Mass Transfer.* **2019**, *140*, 1074–1090.

[56] K. Schladitz, S. Peters, D. Reinel-Bitzer, A. Wiegmann, J. Ohser, *Comput. Mater. Sci.* **2006**, *38*, 56–66.

[57] G. R. Molaeimanesh, H. Saeidi Googarchin, A. Qasemian Moqaddam, *Int. J. Hydrogen Energy.* **2016**, *41*, 22221–22245.

[58] A. Akhgar, PhD thesis, University of Victoria (Canada), **2016**.

[59] X.-D. Niu, T. Munekata, S.-A. Hyodo, K. Suga, *J. Power Sources.* **2007**, *172*, 542–552.

[60] H. Zhang, L. Zhu, H. B. Harandi, K. Duan, R. Zeis, P.-C. Sui, P. Y. A. Chuang, *Energy Convers. Manage.* **2021**, *241*.

[61] L. Zhu, S. Wang, P.-C. Sui, X. Gao, *Int. J. Hydrogen Energy.* **2021**, *46*, 20702–20714.

[62] J. K. Lee, A. Bazylak, *J. Electrochem. Soc.* **2020**, *167*.

[63] J. K. Lee, C. H. Lee, A. Bazylak, *J. Power Sources.* **2019**, *437*.

[64] T. Schuler, J. M. Ciccone, B. Krentscher, F. Marone, C. Peter, T. J. Schmidt, F. N. Büchi, *Adv. Energy Mater.* **2019**, *10*.